

Optical properties of La_2O_3 and HfO_2 for radiative cooling via multiscale simulations

Lihao Wang(王礼浩), Wanglin Yang(杨旺霖), Zhongyang Wang(王忠阳), Hongchao Li(李鸿超), Hao Gong(公昊), Jingyi Pan(潘静怡), Tongxiang Fan(范同祥), and Xiao Zhou(周啸)
Citation: Chin. Phys. B, 2024, 33 (**12**): 127801. DOI: 10.1088/1674-1056/ad84c0
Journal homepage: http://cpb.iphy.ac.cn; http://iopscience.iop.org/cpb

What follows is a list of articles you may be interested in

Design and implementation of the monochromator shielding for the cold neutron spectrometers XINGZHI and BOYA

Jinchen Wang(汪晋辰), Juanjuan Liu(刘娟娟), Daye Xu(徐大业), Florian Grünauer, Lijie Hao(郝丽杰), Yuntao Liu(刘蕴韬), Hongxia Zhang(张红霞), Peng Cheng(程鹏), and Wei Bao(鲍威)
Chin. Phys. B, 2024, 33 (**5**): 057801. DOI: 10.1088/1674-1056/ad3629

Near-field radiative heat transfer between nanoporous GaN films

Xiaozheng Han(韩晓政), Jihong Zhang(张纪红), Haotuo Liu(刘皓佗), Xiaohu Wu(吴小虎), and Huiwen Leng(冷惠文)
Chin. Phys. B, 2024, 33 (**4**): 047801. DOI: 10.1088/1674-1056/ad09a9

Designing radiative cooling metamaterials for passive thermal management by particle swarm optimization

Shenshen Yan(闫申申), Yan Liu(刘岩), Zi Wang(王子), Xiaohua Lan(兰晓华), Yi Wang(汪毅), and Jie Ren(任捷)
Chin. Phys. B, 2023, 32 (**5**): 057802. DOI: 10.1088/1674-1056/acc061

First-principles study on optic-electronic properties of doped formamidinium lead iodide perovskite

Xin-Feng Diao(刁心峰), Yan-Lin Tang(唐延林), Quan Xie(谢泉)
Chin. Phys. B, 2019, 28 (**1**): 017802. DOI: 10.1088/1674-1056/28/1/017802

Linear optical properties of defective KDP with oxygen vacancy: First-principles calculations

Chen Xin (陈鑫), Zhao Qian-Qian (赵倩倩), Wang Xiao-Chun (王晓春), Chen Jun (陈军), Ju Xin (巨新)
Chin. Phys. B, 2015, 24 (**7**): 077802. DOI: 10.1088/1674-1056/24/7/077802

Optical properties of La_2O_3 and HfO_2 for radiative cooling via multiscale simulations

Lihao Wang(王礼浩)[1], Wanglin Yang(杨旺霖)[1], Zhongyang Wang(王忠阳)[1,†], Hongchao Li(李鸿超)[1], Hao Gong(公昊)[1], Jingyi Pan(潘静怡)[1], Tongxiang Fan(范同祥)[1,‡], and Xiao Zhou(周啸)[1,2,§]

[1] *State Key Laboratory of Metal Matrix Composites, School of Materials Science and Engineering, Shanghai Jiao Tong University, Shanghai* 200240, *China*
[2] *Institute of Medical Robotics, Shanghai Jiao Tong University, Shanghai* 200240, *China*

(Received 4 June 2024; revised manuscript received 28 August 2024; accepted manuscript online 9 October 2024)

Radiative cooling materials have gained prominence as a zero-energy solution for mitigating global warming. However, a comprehensive understanding of the atomic-scale optical properties and macroscopic optical performance of radiative cooling materials remains elusive, limiting insight into the underlying physics of their optical response and cooling efficacy. La_2O_3 and HfO_2, which represent rare earth and third/fourth subgroup inorganic oxides, respectively, show promise for radiative cooling applications. In this study, we used multiscale simulations to investigate the optical properties of La_2O_3 and HfO_2 across a broad spectrum. First-principles calculations revealed their dielectric functions and intrinsic refractive indices, and the results indicated that the slightly smaller bandgap of La_2O_3 compared to HfO_2 induces a higher refractive index in the solar band. Additionally, three-phonon scattering was found to provide more accurate infrared optical properties than two-phonon scattering, which enhanced the emissivity in the sky window. Monte Carlo simulations were also used to determine the macroscopic optical properties of La_2O_3 and HfO_2 coatings. Based on the simulated results, we identified that the particle size and particle volume fraction play a dominant role in the optical properties. Our findings underscore the potential of La_2O_3 and HfO_2 nanocomposites for environment-friendly cooling and offer a new approach for high-throughput screening of optical materials through multiscale simulations.

Keywords: radiative cooling, optical properties of La_2O_3 and HfO_2, first-principles calculations, Monte Carlo simulations

PACS: 78.20.–e, 71.15.Mb, 02.70.Uu **DOI:** 10.1088/1674-1056/ad84c0

1. Introduction

The elevation in ground temperatures resulting from the predicament of global warming presents formidable challenges for our society, compelling individuals to adopt cooling techniques, such as air conditioning, to mitigate thermal discomfort. However, these electrical devices collectively account for approximately 15% of the global electricity demand and, in turn, emit approximately 10% of greenhouse gases, thereby exacerbating the global warming predicament.[1,2] To break this vicious cycle, there is an exigent imperative to develop energy-efficient and effective cooling modalities and materials. Recently, passive radiative cooling has emerged as an approach capable of dissipating heat into the frigid expanse of outer space without necessitating energy consumption for cooling attainment.[3–5] This method is promising and has garnered substantial scientific attention because of the zero-energy consumption and remarkable cooling effect. In recent years, passive radiative cooling technologies have already benefited a variety of fields, such as solar cells, personal thermal comfort, and spacecraft thermal control.[6–9] In principle, the efficacy of radiative cooling is heavily dependent on the optical and thermal radiative characteristics of materials, specifically their solar reflectance and infrared emittance.

Pursuing high solar reflectance and infrared emittance of materials is of great importance for achieving high radiative cooling performance. Over the past few years, many new kinds of materials have been used for radiative cooling. For example, Fan *et al*. combined a photonic solar reflector and thermal emitter to achieve radiative cooling using iterated stacking of SiO_2 and HfO_2. This multilayer structure is also known as photonic crystal.[10] Furthermore, many researchers have utilized advanced nanofabrication techniques to form metamaterials with good radiative cooling performance.[11–13] Despite excellent tailoring of the optical and thermal properties of photonic crystals and metamaterials, the fabrication processes are rather complicated, which limits their applicability in large-scale and cost-effective applications. To break off such roadblocks, polymer-based composites are considered potential candidates for radiative cooling because of their superior optical properties and scalable preparation processes.[14,15] However, polymer-based composites usually exhibit a propensity to undergo degradation when subjected to harsh environments, such as high temperatures and ultraviolet (UV) light irradiation.[16,17] This susceptibility results in an elevation in the solar absorption of materials, consequently diminishing

†Corresponding author. E-mail: zy_wang@sjtu.edu.cn
‡Corresponding author. E-mail: txfan@sjtu.edu.cn
§Corresponding author. E-mail: zhouxiao113@sjtu.edu.cn

© 2024 Chinese Physical Society and IOP Publishing Ltd

their cooling efficacy.

It is also worth noting that inorganic oxides (e.g., binary oxides consisting of TiO_2, rare-earth (RE) oxides Y_2O_3, and RE_6MoO_{12}) have sparked increasing scientific attention for radiative cooling applications.[18,19] Such inorganic pigments composed of oxides exhibit both robust optical properties and good durable stability compared to their pure organic counterparts.[20] For instance, currently reported inorganic pigments with RE_6MoO_{12} microparticles exhibit robust optical properties and radiative cooling performance.[21] In parallel, microporous glass coatings containing binary oxides of SiO_2 and Al_2O_3 enable large temperature decreases in harsh environments. These results further suggest that these simple inorganic oxides show high solar reflectance and midinfrared emissivity.[22] Despite numerous oxides, potential candidates for white coatings remain unexplored. Currently, the discovered white coatings with oxide particles suffer from undesirable solar reflectance and infrared emittance. To screen the optimal oxide candidates for radiative cooling, some important criteria regarding intrinsic material properties must be satisfied. The first rule of thumb is inherent bandgap and refractive indices. To increase the solar reflectance, the bandgap of the selected material should be large enough so as to eliminate ultraviolet absorption as much as possible. Meanwhile, the lattice vibration and dispersion must be carefully considered because of the vital role of phonon property in the linewidth of infrared emittance and in the dispelling of high reflectance Reststrahlen band. These two important and stringent prerequisites clearly suggest that the search for inorganic oxides with high solar reflectance and infrared emittance remains a challenging task.

Within the diverse landscape of oxide families, La_2O_3 and HfO_2 are two representatives of RE and third-to-fourthsubgroup oxides, respectively, which are distinguished by their exceptional spectral selectivity.[23–25] These two representative oxides are well suited for applications in radiative cooling, given their elevated dielectric permittivity ($\varepsilon' > 20$),[26,27] broad bandgap ($E_g \geq 5.3$ eV),[28,29] high refractive index ($n > 1.8$),[30] robust thermal stability, and cost-effective fabrication processes. However, the intrinsic optical properties of La_2O_3 and HfO_2 have only been reported within a very narrow spectrum in the literature, and those in the wide spectrum (especially in the infrared regime) are still lacking, which severely hampers the deep understanding of radiative cooling performance. Such intrinsic optical constants over a wide spectrum are directly correlated with atomistic configuration/electronic structure/lattice vibrations at the atomic scale, which are determined by solar reflectance and infrared emittance. On the other hand, the distribution and arrangement of particles at macroscale also play a significant role in light scattering. Thus, scattering behavior undoubtedly affects the optical properties of La_2O_3 and HfO_2. However, to the best of our knowledge, no systematic studies on the intrinsic properties at the atomic scale and optical performance at the macroscale have been documented for either La_2O_3 or HfO_2, and not only the effect of particle size/distribution on the optical properties.

The forgoing absence of intrinsic optical constants at the atomic scale and inadequate understanding of light scattering behavior at the macroscale motivated us to comprehensively investigate La_2O_3 and HfO_2 using multiscale simulations in this study. Many researchers have used multiscale simulations to obtain the radiation properties of materials at different scales. Tong *et al.* used the self-consistent quasiparticle GW (sc-QPGW) method to accurately predict the bandgap of $BaSO_4$, and Monte Carlo (MC) simulations were used to understand the effect of thickness on the optical properties of $BaSO_4$-acrylic nanocomposites.[31] This study demonstrates that the combination of MC simulation and first-principles calculations can quickly obtain the radiation properties of specific materials; however, it does not discuss other important structural parameters of composite materials, such as the influence of particle size and volume fraction on optical properties. Joseph *et al.* studied the influence of different particle diameters on the optical properties of a TiO_2 nanoparticle-acrylic system via MC simulations.[32] This study provides a good way to use MC simulations to study the effects of different structural parameters on the radiation properties of materials. However, the dielectric properties of TiO_2 come from experimental values. Compared with the results of first-principles calculations, the results are affected by the experimental conditions and are not suitable for high-throughput screening applications.

In our study, first-principles calculations were used to obtain the dielectric function of La_2O_3 and HfO_2 over a wide spectrum. The Bethe–Salpeter equation (BSE) was solved to describe the photon–electron interactions in the solar spectrum, while lattice dynamics calculations were performed to describe the photon–phonon interactions in the infrared spectrum.[33] Once the optical constants in a wide range spectrum are obtained, these properties can be fed into MC simulations to achieve light scattering behavior and macroscopic optical properties (i.e., reflectance, emittance, etc.) of La_2O_3 and HfO_2 to determine the optimal structural parameters (i.e., particle diameter, volume fraction, and thickness). The multiscale predictive framework adopted in this study would help us better understand the underlying physics of the optical properties of La_2O_3 and HfO_2.

2. Methodology

2.1. First-principles calculations

In this study, we used the first-principles method to calculate the dielectric function for both solar and infrared spectra. As for the solar spectrum, electronic transition contributes to photon absorption. By aggregating all conceivable vertical transitions spanning the bandgap, the imaginary component $\varepsilon''(\omega)$ of the dielectric constant as a function of frequency ω can be ascertained using Fermi's golden rule[34]

$$\varepsilon''(\omega) = \frac{4\pi^2 e^2}{V_0} \lim_{q\to\infty} \frac{1}{q^2} \sum_{c,\upsilon,k} 2\omega_k \delta(\tau_{ck} - \tau_{\upsilon k} - \omega) \times \langle u_{ck+e_\alpha q} | u_{\upsilon k} \rangle \langle u_{ck+e_\beta q} | u_{\upsilon k} \rangle, \quad (1)$$

where e_α and e_β are the unit vectors in the α and β directions, respectively. V_0 is the volume of unit box; ω_k and τ are weighting factors for k point in Brillouin zone and electron energy. The periodic cell of the orbitals at k point is illustrated by u_{ck}. The conduction and valance bands are marked by the symbols c and υ, respectively. The real part $\varepsilon'(\omega)$ of the dielectric function can then be calculated in accordance with Kramers–Krönig transformation[35]

$$\varepsilon'(\omega) = 1 + \frac{2}{\pi} P \int_0^\infty \frac{\varepsilon''(\omega')\omega'}{\omega'^2 - \omega^2} \mathrm{d}\omega', \quad (2)$$

where P is the Cauchy principal value of the integral.

With respect to infrared spectrum, the dielectric function can be expressed as[36]

$$\frac{\varepsilon(\omega)}{\varepsilon_\infty} = \prod_g \frac{\omega_{g,\mathrm{LO}}^2 + \mathrm{i}\gamma_{g,\mathrm{LO}}\omega - \omega^2}{\omega_{g,\mathrm{TO}}^2 + \mathrm{i}\gamma_{g,\mathrm{TO}}\omega - \omega^2}, \quad (3)$$

where the indices LO and TO are the longitudinal and transverse optical phonon modes, respectively; ω_g denotes the lattice resonance frequency, where g represents the g infrared active mode; γ_g is the phonon damping factor, which can be obtained by an anharmonic lattice dynamics approach; and ε_∞ is the high-frequency dielectric constant. In this study, we considered three-phonon scattering (3ph) into consideration (i.e., $\gamma_g = \gamma_g^{3\mathrm{ph}}$). All calculations were carried out using the Vienna *Ab initio* Simulation Package (VASP),[37] which has implemented the projected augmented waves (PAW) method, and the electron exchange and correlation functionals were described by the generalized gradient approximation (GGA) with a specific Perdew–Burke–Ernzerhof (PBE) function.[38] As for the electronic structure calculation, it is worth noting that the conventional PBE method underestimates the bandgap. To address this issue, we adopted the hybrid functionals proposed by Heyd, Scuseria, and Ernzerhof (i.e., HSE06).[39] The cutoff energy was set at 520 eV. The convergence criteria for the energy and atomic force were 1×10^{-8} eV and 1×10^{-6} eV/Å, respectively. The Monkhorst pack/Γ-centered k mesh was adopted to sample the Brillouin zone, where $9\times9\times4$ and $5\times5\times5$ grid meshes were used for La_2O_3 and HfO_2, respectively. Furthermore, the density functional perturbation theory (DFPT) implemented in the Phonopy package was used for the extraction of second-order interatomic force constants (IFCs), whereas the third-order IFCs were calculated using the THIRDORDER.PY package.[40] The three-phonon scattering damping factor of each infrared active mode was determined using the Sheng-BTE package.[41] Using this strategy, a complex dielectric function for both solar and infrared spectra was achieved. The complex refractive indices n and k can then be calculated via $\varepsilon = (n + \mathrm{i}k)^2$.

2.2. Monte Carlo simulations

After obtaining the intrinsic refractive indices n and k, the macroscopic optical properties of La_2O_3 and HfO_2 nanocomposites with the format of coatings/paints were calculated using MC simulations. In particular, the scattering (Q_{sca}), extinction (Q_{ext}), and absorption (Q_{abs}) coefficients that were used as input parameters in the MC simulations were calculated using the Lorenz–Mie scattering theory[42]

$$\begin{aligned} Q_{\mathrm{sca}}(m,\chi) &= \frac{2}{\chi^2}\sum_{n=1}^{\infty}(2n+1)\left(|a_n|^2 + |b_n|^2\right), \\ Q_{\mathrm{ext}}(m,\chi) &= \frac{2}{\chi^2}\sum_{n=1}^{\infty}(2n+1)\,\mathrm{Re}\{a_n + b_n\}, \\ Q_{\mathrm{abs}} &= Q_{\mathrm{ext}}(m,\chi) - Q_{\mathrm{sca}}(m,\chi), \\ a_n &= \frac{m\psi_n(m\chi)\psi_n'(\chi) - \psi_n(\chi)\psi_n'(m\chi)}{m\psi_n(m\chi)\xi_n'(\chi) - \psi_n'(m\chi)\xi_n(\chi)}, \\ b_n &= \frac{\psi_n(m\chi)\psi_n'(\chi) - m\psi_n(\chi)\psi_n'(m\chi)}{\psi_n(m\chi)\xi_n'(\chi) - m\xi_n(\chi)\psi_n'(m\chi)}, \end{aligned} \quad (4)$$

where ψ_n is the Riccati–Bessel function, and χ is the size parameter, being defined as $\pi D/\lambda$ (D is the particle diameter, and λ is the wavelength); $m = (n + \mathrm{i}k)/n$ is the normalized complex refractive index using the DFT calculated n and k of particle (where n_0 is the refractive index of matrix). These optical parameters from the Mie theory were fed into the MC simulations to effectively track light propagation. In particular, the radiative transfer equation (RTE) was solved using the MC approach, and the photons for reflectance, transmittance, and absorptance can be statistically evaluated. To reach good statistical convergence, we used 5×10^5 launched photons, and the thickness of the coating was selected to be 50–800 μm.

3. Results and discussion

The prototypical crystal structures of La_2O_3 and HfO_2 examined in this study were $p\bar{3}m1$ and $P2_1/c$, respectively, because these structures are stable at room temperature.[43,44] The primitive cells of La_2O_3 and HfO_2 contained 5 and 12 atoms, respectively, as shown in Fig. 1. After careful structure relaxation, we finally got the optimized lattice constants

($a = b = 3.94$ Å and $c = 6.18$ Å for La_2O_3; $a = 5.14$ Å, $b = 5.18$ Å, and $c = 5.32$ Å for HfO_2), as shown in Table 1. These calculated lattice constants are in good agreement with the previously reported data.

Table 1. Calculated lattice constants and bandgaps of La_2O_3 and HfO_2 compared to previously reported data (parentheses).

Materials	Lattice parameters			Bandgap (eV)
	a (Å)	b (Å)	c (Å)	
La_2O_3	3.94 (3.93[45])	3.94 (3.93[45])	6.18 (6.13[45])	5.39 (5.30[46])
HfO_2	5.14 (5.10[47])	5.18 (5.26[47])	5.32 (5.28[47])	5.89 (5.8[28])

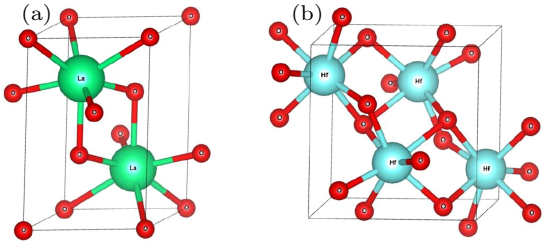


Fig. 1. Atomic structures of the examined primitive unit cells: (a) La_2O_3 and (b) HfO_2.

Figure 2 shows the calculated band structures and density of states (DOS) for La_2O_3 and HfO_2. Notably, the conventional PBE function underestimates the bandgap (i.e., 3.94 eV and 4.32 eV for La_2O_3 and HfO_2, respectively). To address this issue and calibrate the band structures, we adopted the HSE06 instead of the PBE functional, and the final calculated bandgaps were 5.39 eV and 5.89 eV for La_2O_3 and HfO_2, respectively (see Figs. 2(c) and 2(d), which are consistent with other theoretical calculations in the literature (see Table 1).[28,46] Such an agreement not only gives rise to the validation of our DFT calculations but also provides an important foundation for the following calculations of dielectric functions and corresponding intrinsic optical properties of La_2O_3 and HfO_2 in the full UV-VIS-IR regime. Another intriguing aspect is that we observed bandgaps for both examined materials that are much larger than the energy spectrum for photon absorption in the range of 0.25–2.5 μm, which indicates no absorption in the solar spectrum.

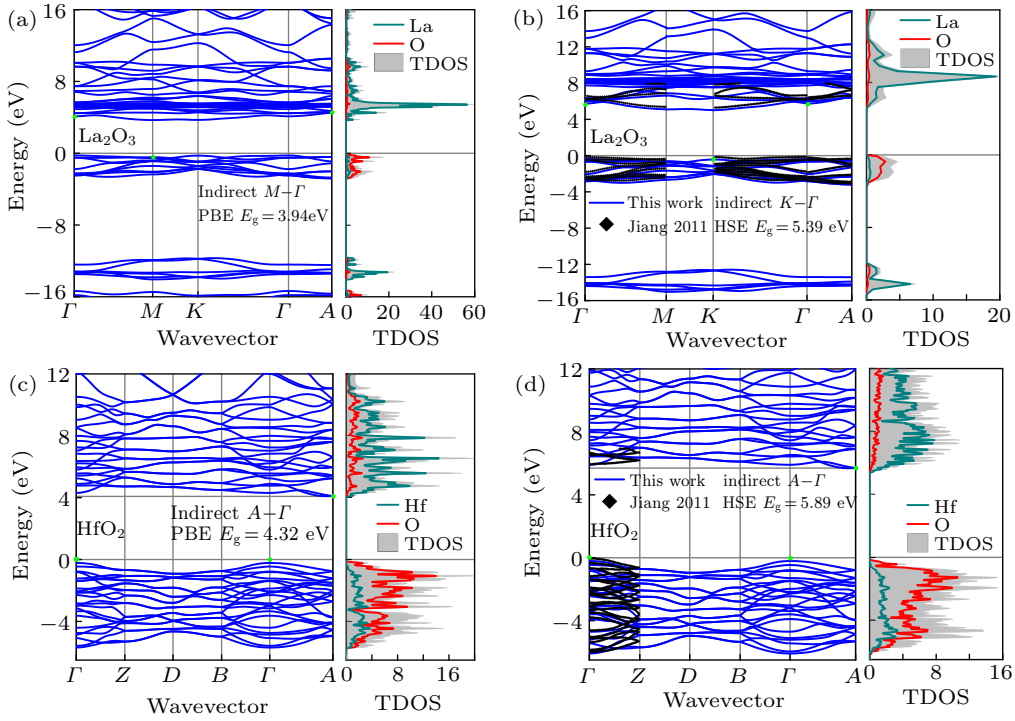


Fig. 2. Calculated band structure for (a) La_2O_3 using PBE functional, (b) La_2O_3 using HSE06 functional, (c) HfO_2 using PBE functional, and (d) HfO_2 using HSE06 functional.

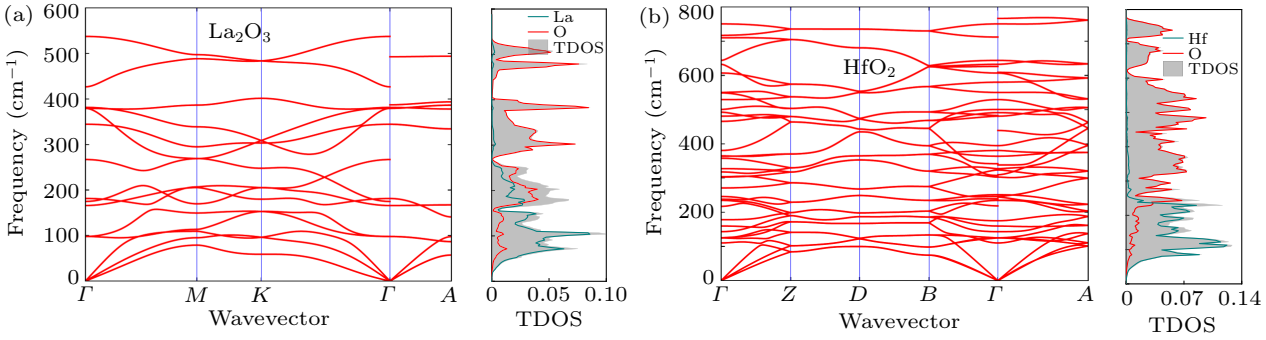


Fig. 3. Calculated phonon dispersion and phonon DOS for (a) La_2O_3 and (b) HfO_2.

In addition to the electronic band structures, we scrutinized the phonon dispersion along a highly symmetrical propagation direction using DFPT, as shown in Fig. 3. Based on the calculated phonon dispersion, we first noted that the examined crystal structures of La_2O_3 and HfO_2 were both stable due to the lack of negative (image) frequency. It is also worth noting that both La_2O_3 and HfO_2 were polarized. Thus, nonanalytical terms must be considered in the calculation of phonon dispersion.

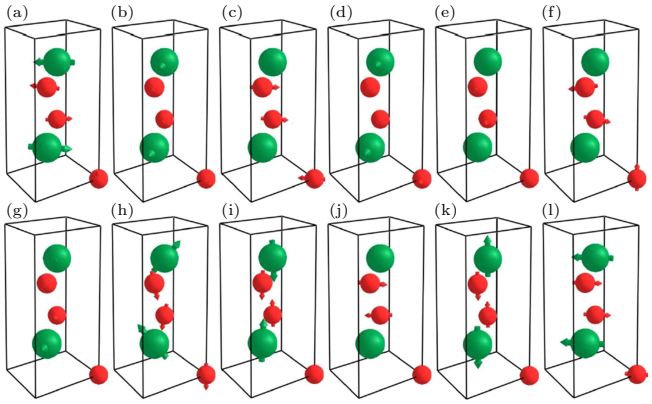


Fig. 4. Infrared active phonon vibrational modes of La_2O_3 with A_{2u} symmetry arranged in order of increasing frequency, with (a)–(f) corresponding to the TO modes and (g)–(l) corresponding to the LO modes. Green atoms indicate lanthanum, red atoms indicate oxygen, and arrows correspond to the direction of atomic movement.

In light of the phonon dispersion calculations, a series of zero-center (i.e., Γ point) optical modes can be identified in accordance with the irreducible representation. With the assistance of space-group theory analysis, the infrared (IR) active modes for La_2O_3 and HfO_2 are denoted as $\Gamma_{\mathrm{IR}} = 4A_{2u} + 4E_u$ and $\Gamma_{\mathrm{IR}} = 35A_u + 34B_u$, respectively. Longitudinal (LO) and transverse (TO) wave branches exist for each optical mode. In particular, the LO branches can be categorized into strong and weak modes according to the atomic displacements. The strong mode results in a strong electric field and renders the frequency of LO higher than that of the TO branch. As for the weak mode, the tiny oscillation of atom induces only a very weak electric field. The lattice vibrations of both La_2O_3 and HfO_2 in terms of the IR-active modes can be visualized using V_sim software[48] (see Figs. 4–7).

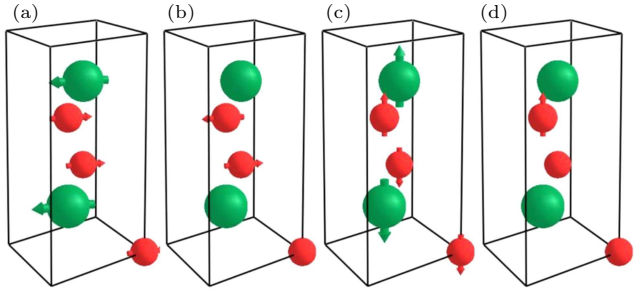


Fig. 5. Infrared active phonon vibrational modes of La_2O_3 with E_u symmetry arranged in order of increasing frequency, with (a)–(b) corresponding to the TO modes and (c)–(d) corresponding to the LO modes. Green atoms indicate lanthanum, red atoms indicate oxygen, and arrows correspond to the direction of atomic movement.

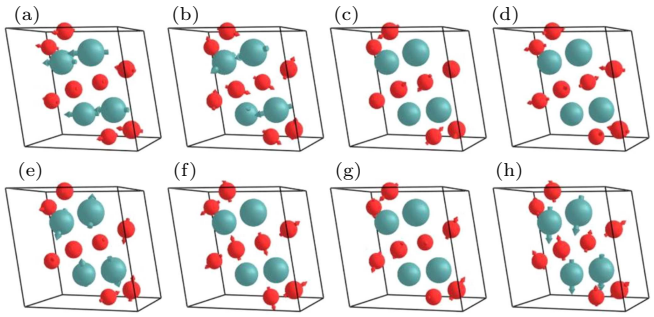


Fig. 6. Infrared active phonon vibrational modes of HfO_2 with A_u symmetry arranged in order of increasing frequency, with (a)–(d) corresponding to the TO modes and (e)–(h) corresponding to the LO modes. Blue atoms indicate hafnium, red atoms indicate oxygen, and arrows correspond to the direction of atomic movement.

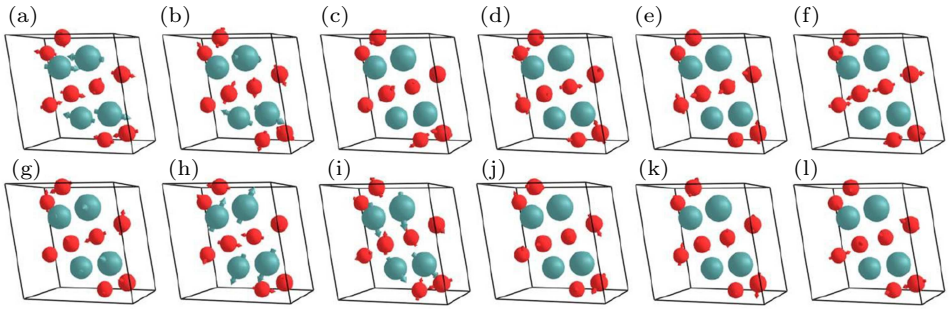


Fig. 7. Infrared active phonon vibrational modes of HfO_2 with B_u symmetry arranged in order of increasing frequency, with (a)–(f) corresponding to the TO modes and (g)–(l) corresponding to the LO modes. Blue atoms indicate hafnium, red atoms indicate oxygen, and arrows correspond to the direction of atomic movement.

In addition, the polarization induced by atomic displacement leads to LO–TO splitting at the Γ point of the Brillouin zone, as illustrated in Fig. 3. In addition to analyzing lattice vibrational patterns, we also calculated the frequency and damping factor of each IR-active mode using first-principles calculations, which fully accounted for two-phonon and three-phonon (i.e., 2ph and 3ph) scattering. The calculated parameters, including the phonon frequencies and damping factors of the identified IR modes, are listed in Table 2. To the best of our knowledge, this is the first study to complete phonon-related parameters using first-principles calculations, which provides atomistic insight toward a better understanding of IR phonon characteristics in La_2O_3 and HfO_2. Moreover, the calculated high-frequency dielectric constants ε_∞ are 4.80 (4.924[29]) and

4.89 for La_2O_3 and HfO_2, respectively. These necessary parameters can be fed into Eq. (3) to obtain the dielectric functions and the corresponding intrinsic optical properties in the mid-IR spectrum.

Table 1. Calculated phonon frequencies and damping factor of each active mode for La_2O_3 and HfO_2, and the experimentally reported data are also listed in parentheses.

Material	IR-active modes		DFT in this study (experiment) (cm^{-1})			
	Type	g	$\omega_{g,TO}$	$\gamma_{g,TO}$	$\omega_{g,LO}$	$\gamma_{g,LO}$
La_2O_3	A_{2u}	1	97.63	3.49	98.74	2.97
		2	168.40	8.86	177.17	9.52
		3	180.60 (204.2[29])	10.04	264.81	11.56
		4	344.84 (354[49])	7.77	369.25 (376.9[29])	12.74
		5	379.95	10.30	380.54 (374[49])	10.07
		6	433.54 (445.7[29])	43.84	535.89 (517.6[29])	6.71
	E_u	1	165.79 (199.4[29])	9.04	180.73 (204.2[29])	9.44
		2	379.72 (376.9[29])	12.27	492.60 (397.4[29])	24.32
HfO_2	A_u	1	98.19	0.83	133.35 (123[47])	2.52
		2	394.34 (391[47])	15.48	445.16	17.74
		3	468.31 (456[47])	20.79	493.18 (478[50])	10.72
		4	567.38 (577[47])	19.97	625.26 (634[47])	15.72
	B_u	1	101.78 (104[51])	1.39	141.08	1.84
		2	189.95 (180[50])	2.00	198.82 (192[51])	4.05
		3	285.99 (270[51])	4.50	317.38 (300[47])	24.44
		4	463.83 (414[47])	13.34	464.84 (449[47])	13.78
		5	479.65 (494[47])	19.20	503.43 (553[47])	15.83
		6	704.80 (694[47])	19.28	735.68 (740[51])	20.93

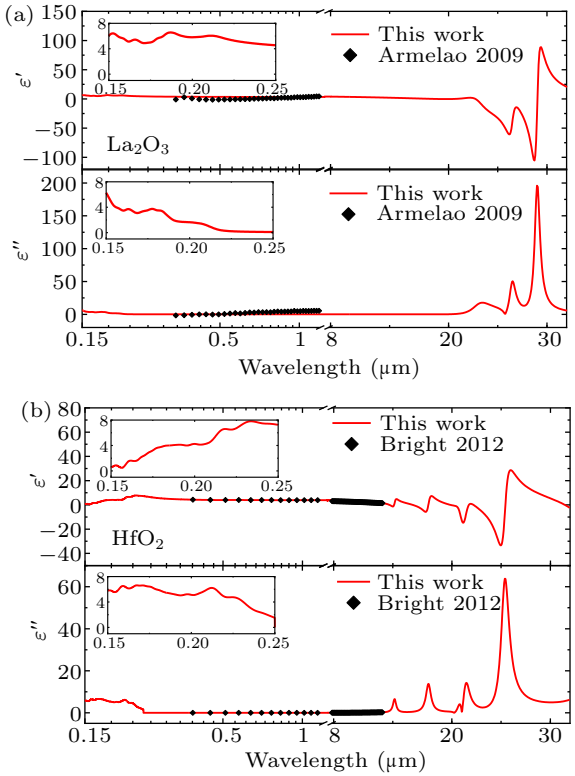


Fig. 8. Calculated dielectric function for La_2O_3 and HfO_2 from the UV to IR spectrum. The experimental data of La_2O_3 and HfO_2 are also marked by black diamond dots. The real and imaginary parts of the dielectric function for (a) La_2O_3 and (b) HfO_2.

The dielectric function from the UV to IR spectrum is shown in Fig. 8. As for the solar spectrum, the dielectric function experiences fluctuation in the UV range, followed by a stable plateau around 0.25 μm and 1 μm for La_2O_3 and HfO_2 systems, respectively, in VIS-NIR spectrum. In the mid-IR range, the wavelength-dependent dielectric function can be calculated using Eq. (2). For La_2O_3, there are three oscillators with wave values of 433 cm^{-1}, 379 cm^{-1}, and 346 cm^{-1}, corresponding to the resonance peaks located at 23.4 μm, 26.5 μm, and 28.9 μm. These phonon resonance peaks would result in a strong absorption in the IR regime. Regarding HfO_2, there were five oscillators with wave values of 704 cm^{-1}, 567 cm^{-1}, 479 cm^{-1}, 468 cm^{-1}, and 394 cm^{-1}, corresponding to the resonance peaks located at 14.2 μm, 17.6 μm, 20.8 μm, 21.5 μm, and 25.4 μm. The corresponding IR spectrum is spanned from 13.5 μm to 29.5 μm, being slightly boarder than that of La_2O_3. We also found that the calculated dielectric function of HfO_2 was consistent with the available experimental data,[52] demonstrating the accuracy of our calculations.

In addition, we uncovered no phonon resonance in the 8–13 μm band for both La_2O_3 and HfO_2. Therefore, we deemed that the strong absorption induced by phonon resonance might not be drastically attributed to the emissivity in the 8–13 μm sky window.

Once obtained, the dielectric function, refractive index, and extinction coefficients (i.e., n and k) can then be calculated using the formula $\varepsilon = (n + ik)^2$.[53] The calculated complex refractive indices of La_2O_3 and HfO_2 are shown in Fig. 9. Our predictions for the optical constants of these two materials are in good agreement with the data reported in the literature. The experimental complex dielectric function of La_2O_3 shown in Fig. 8 was obtained by fitting the ellipsometry test results using the Lorentz single oscillator model.[54] The ex-

perimental refractive index of the La_2O_3 film in Fig. 9 was obtained by measuring the transmittance and emissivity, obtaining the refractive index data using the spectroreflectometry method,[55] and fitting the Sellmeir dispersion equation with the regression equation.[56] The Cauchy formula was combined with the Lorentz multi-oscillator model to fit the HfO_2 film transmittance and reflectance data obtained from experimental tests.[52] The experimental complex dielectric function data of HfO_2 (Fig. 8) were obtained, and the experimental complex refractive index data (Fig. 9) were calculated using the aforementioned formula.

We believe that this scenario is due to the negative correlation between the bandgap and refractive index of the semiconductor. Meanwhile, the sufficiently large bandgap of both oxides would result in k being close to zero, which agrees well with other reported data in the literature. Compared to conventional materials, such as TiO_2 with a smaller bandgap, the larger bandgaps of La_2O_3 and HfO_2 can further reduce the absorption in the UV band and achieve high reflectivity in the solar band.

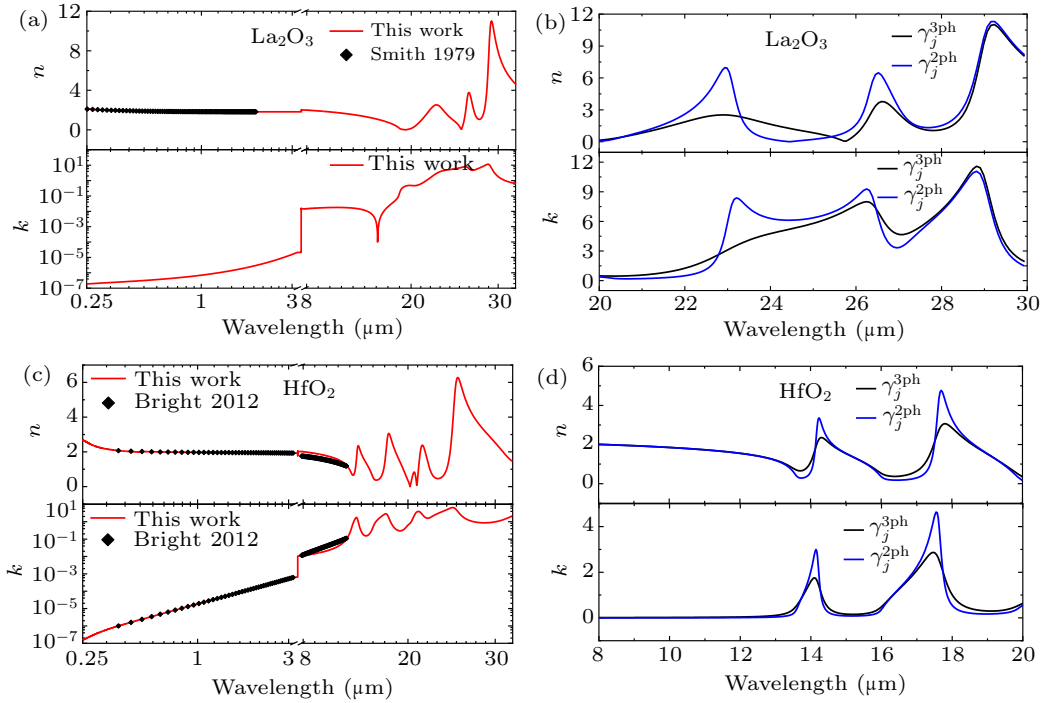


Fig. 9. Calculated complex refractive indices n and k of (a) La_2O_3 and (c) HfO_2. The black diamonds indicate experimental data from the UV to IR spectrum regime. (b) and (d) Calculated n and k by considering the 2ph and 3ph scattering in the IR range.

As mentioned in the previous section, 3ph scattering is fully considered in phonon calculations. Based on the calculated results, we found that the complex refractive index shows a wider range and a relatively smooth peak than the 2ph scattering effect. Such a scenario would result in a higher emissivity in the IR regime. Consequently, the influence of 3ph scattering cannot be simply neglected. Figures 9(b) and 9(d) show a comparison of the calculated n and k by considering 2ph and 3ph scattering for La_2O_3 and HfO_2. As shown in Fig. 9, we identified different peaks of intrinsic n and k parameters for both La_2O_3 and HfO_2, where the range of identified peaks for La_2O_3 is far from that for HfO_2. This result also indicates that the range of high IR emissivity in La_2O_3 is greater than that in HfO_2. This scenario was also confirmed by the theoretically calculated normal reflectance using Fresnel's formula (see Fig. 10). Meanwhile, our analysis revealed that both La_2O_3 and HfO_2 exhibit relatively low reflectance in the solar spectrum. However, regions of high reflectance were distinctly observed in the mid-IR range, corresponding to the Reststrahlen band.[57,58]

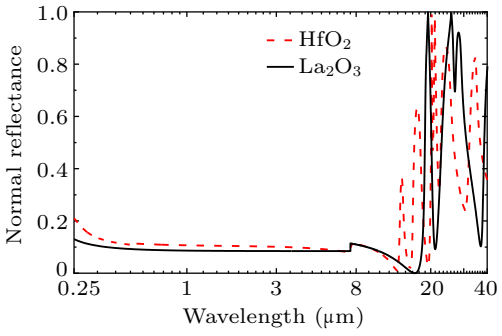


Fig. 10. Normal reflectance obtained using Fresnel's equation for La_2O_3 and HfO_2.

Following the determination of the complex refractive index of nanoparticles across the entire wavelength range through first-principles calculations, we investigated composites comprising La_2O_3 (or HfO_2) nanoparticles dispersed in a representative acrylic matrix (refractive index n_0 of the acrylic matrix set to 1.5) to ascertain the macroscopic optical proper-

ties. The Mie scattering theory was initially applied to calculate the scattering and absorption coefficients of individual particles. Subsequently, the optical characteristics of the composites, such as reflectance and absorbance, were derived by solving the RTE using the MC method. It is worth noting that this approach enables the prediction of reflectance, absorptivity, and transmittance of nanoparticle–polymer composites, for which the inherent optical constants are unknown. Furthermore, this method can facilitate the optimization of parameters, such as material selection, particle size distribution, volume concentration, and composite thickness, to achieve the desired spectral response with high efficiency.

To further refine the optical properties of the nanocomposites, we simulated samples with various particle sizes d (0.1–0.8 μm), volume fractions f_v (10%–80%), and thicknesses h (50–800 μm). The impact of these parameters on the optical properties was comprehensively analyzed, where the optimal optical properties were achieved for a particle diameter of 0.6 μm, volume fraction of 40%, and thickness of 400 μm. In the following section, the influence of each parameter on the optical properties of nanocomposites is discussed in detail.

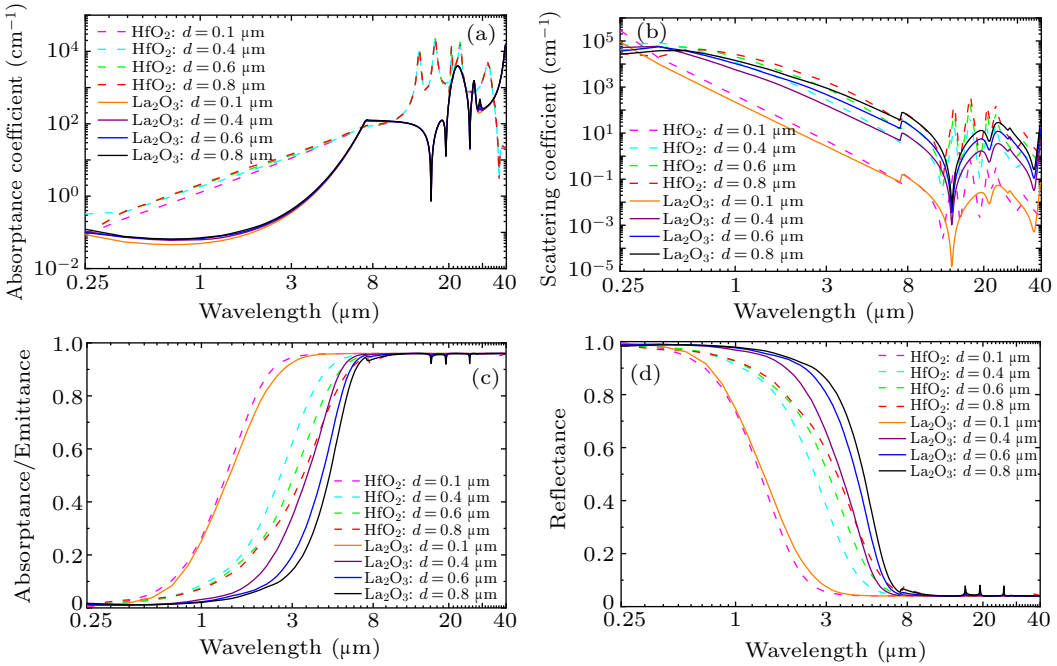


Fig. 11. Optical characteristics and corresponding optical properties of La_2O_3 and HfO_2 nanocomposites of various particle sizes with a fixed volume fraction ($f_v = 40\%$) and thickness ($h = 400$ μm). (a) Absorption coefficients of La_2O_3 and HfO_2 nanocomposites. (b) Scattering coefficients of La_2O_3 and HfO_2 nanocomposites. (c) Absorptance/emissivity of La_2O_3 and HfO_2 nanocomposites. (d) Reflectance of La_2O_3 and HfO_2 nanocomposites.

Figure 11 illustrates the absorption coefficient, scattering coefficient, absorptivity, and reflectivity for nanocomposites consisting of La_2O_3 (or HfO_2) with a volume fraction of 40% and a thickness of 400 μm. In particular, the particle size was varied from 0.1 μm to 0.8 μm. As shown in Figs. 11(a) and 11(b), the absorption coefficients of nanoparticles of the same material but different particle diameters are essentially consistent across the entire spectral range, indicating that the absorption properties are largely independent of nanoparticle size. We observed that both materials exhibit high scattering performance in the solar spectrum (0.25–2.5 μm) and high absorption coefficients in the atmospheric window spectrum (8–13 μm), demonstrating their suitability for radiative cooling applications. Additionally, the scattering coefficient of nanoparticles of the same material increases with the particle size. The likelihood of particles reflecting photons can be explained by their ability to backscatter photons, and the scattering phase function helps to visualize this capability. When considering spheres interacting with photons, three main scattering regimes are defined: Rayleigh scattering, Mie scattering, and geometric scattering. In the Mie scattering regime, particles with sizes comparable to the wavelength of light exhibit a predominantly backward-weighted scattering phase function. Rayleigh scattering occurs when the particles are much smaller than the wavelength of light, resulting in more equivalent forward and backward scattering phase functions. Geometric scattering, which occurs when particles are much larger than the wavelength of light, produces a significant forward scattering phase function with a distinct narrow backward scattering region. For the solar radiation spectrum (0.25–2.5 μm), where the incident energy is most concentrated, smaller-diameter particles (0.1 μm) primarily produce Rayleigh scattering, resulting in equivalent forward and backward scattering that cancels each other out, leading to weaker scattering coefficients. Larger-diameter particles (0.4–0.8 μm) mainly produce Mie scattering, causing the signifi-

cant backward scattering, thereby increasing their scattering coefficients continuously with increasing diameter. To more accurately compare the impact of different parameters on the optical properties of the composites, we used AM1.5 spectral data to calculate the absorptance under the solar spectrum (α_s) and emissivity (ε) under the atmospheric window, as presented in Table 3. It was observed that for larger particle diameters (i.e., 0.4 μm, 0.6 μm, and 0.8 μm), the enhancement effect of the scattering coefficient is not pronounced. For instance, the changes in absorptance and emittance for a particle diameter of 0.8 μm are negligible compared to those for a diameter of 0.6 μm.

As depicted in Figs. 11(c) and 11(d), the absorptivity and reflectivity of the composites were positively correlated with the intermediate parameters of individual particles (i.e., the absorption coefficient and scattering coefficient). Consequently, an increase in the particle diameter led to an increase in reflectivity and a decrease in absorptivity. Notably, the absorption coefficient was positively correlated with the extinction coefficient (k) whereas the scattering coefficient was positively related to the refractive index (n). As demonstrated in Figs. 9(a)–9(c), within the solar spectrum range, La_2O_3 with a lower bandgap exhibited a higher refractive index and lower extinction coefficient than HfO_2. Therefore, at each particle size, La_2O_3 has a higher absorption coefficient and a lower scattering coefficient than HfO_2, highlighting the influence of the particle type on the optical properties.

Table 3. Calculated solar absorptance (α_s) and emissivity (ε) under the sky window for various structural parameters of La_2O_3 and HfO_2 based on AM1.5 spectral data.

Parameters (d and h in units of μm)		La_2O_3		HfO_2	
		α_s (0.25–2.5 μm)	ε (8–13 μm)	α_s (0.25–2.5 μm)	ε (8–13 μm)
$f_v = 40\%$, $h = 400$	$d = 0.1$	0.1179	0.96	0.1296	0.96
	$d = 0.4$	0.0393	0.9599	0.0448	0.9590
	$d = 0.6$	0.0137	0.9572	0.0408	0.9569
	$d = 0.8$	0.0127	0.9539	0.0407	0.9532
$d = 0.6$, $h = 400$	$f_v = 10\%$	0.0567	0.9575	0.0524	0.9573
	$f_v = 40\%$	0.0137	0.9572	0.0408	0.9569
	$f_v = 60\%$	0.0117	0.9572	0.0392	0.9569
	$f_v = 80\%$	0.0112	0.9572	0.0384	0.9569
$d = 0.6$, $f_v = 40\%$	$h = 50$	0.0332	0.9574	0.1453	0.9582
	$h = 400$	0.0137	0.9572	0.0408	0.9569
	$h = 600$	0.0125	0.9572	0.0408	0.9569
	$h = 800$	0.0122	0.9572	0.0409	0.9569

In addition to particle size, the impact of volume fraction on the optical properties of the nanocomposites was systematically studied. As shown in Figs. 12(a) and 12(b), an increase in the volume fraction of nanoparticles essentially equates to an increase in their total number. This elevation leads to a significant effect: a boost in the total number of particles contributes to scattering and absorption, resulting in a corresponding increase in both the absorption coefficient and scattering coefficient with the increase in volume fraction. Analogous to the trend observed for particle size, the impact on the enhancement of optical properties diminished as the volume fraction increased. Table 3 also presents the absorptance in the solar spectrum range and emissivity in the atmospheric window for both types of particles at varying volume fractions. Specifically, the solar band absorption of La_2O_3 decreased by 0.0005, and the atmospheric window emissivity decreased by 0.0001 for a volume fraction of 60% compared with 80%. For La_2O_3, the absorption in the solar spectrum range decreased by only 0.0008, whereas the emissivity in the atmospheric window remained unchanged. Figures 12(c) and 12(d) present the absorptance and reflectance of La_2O_3 and HfO_2 at various volume fractions. It is evident that, as the volume fraction increases, the reflectance increases, whereas the absorptivity decreases. Moreover, we observed that for HfO_2 with a lower refractive index at a volume fraction of 60%, the absorption coefficient was higher and the scattering coefficient was lower, manifesting in the optical properties of enhanced absorption and reduced reflectance.

In addition to the particle size and volume fraction, we thoroughly explored the optical properties of nanocomposites with varying coating thicknesses. Figures 13(a) and 13(b) illustrate the trends in the absorption and scattering coefficients across different thicknesses (ranging from 50 μm to 800 μm). Given that the absorption and scattering coefficients of the single-particle system are independent of the film thickness, the coefficients of the nanocomposites remained consistent across different thicknesses. However, the increased thickness hampered photon transmission through the material, causing a gradual decrease in transmittance during the MC simulations. In the solar spectrum, both La_2O_3 and HfO_2 exhibited high scattering and low absorption, leading to a higher likelihood of photon scattering. As thickness increased, the optical path lengthened, which enhanced the number of photon interactions with the material and the overall scattering behavior. This increase in scattering led to reduced absorption and photon transmission. Macroscopically, this translates into a

decrease in transmittance with increasing thickness, with the reduced transmittance being predominantly converted into reflectance in the high scattering regime. In the mid-IR band, absorptivity remains largely unaffected by thickness due to the high absorption properties of the material, resulting in the absorption of photons shortly after entering the material. Our comprehensive analysis of the forgoing sections fully demonstrates that the effect of scattering induced by multiple particles plays a vital role in the macroscopic optical properties of La_2O_3 and HfO_2. Compared to the intrinsic optical properties calculated using Fresnel's equation (see Fig. 10), the scattering of particles can change and even invert the optical response in both the solar and mid-IR spectra. Consequently, the optical properties of nanocomposites can be macroscopically tuned by ingeniously optimizing the structural parameters, including the particle distribution, volume fraction, and topological configurations, which are highly advantageous for the design and optimization of nanocomposites with robust optical properties.

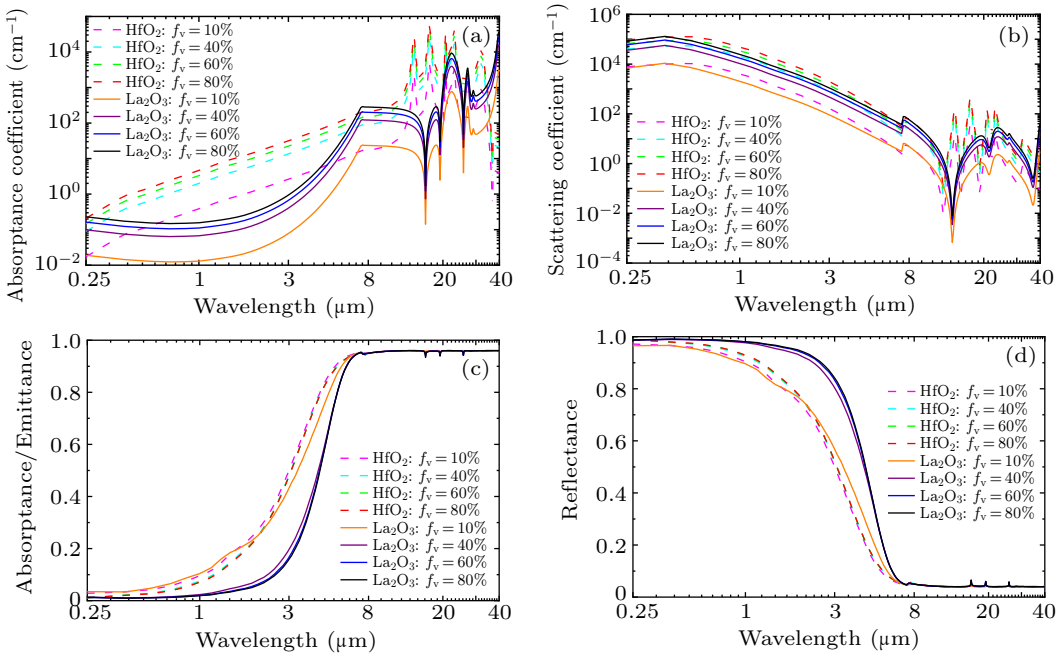


Fig. 12. Optical characteristics and corresponding optical properties of La_2O_3 and HfO_2 nanocomposites at various volume fractions with a fixed particle size ($d = 0.6$ μm) and thickness ($h = 400$ μm). (a) Absorption coefficients of La_2O_3 and HfO_2 nanocomposites. (b) Scattering coefficients of La_2O_3 and HfO_2 nanocomposites. (c) Absorptance/emissivity of La_2O_3 and HfO_2 nanocomposites. (d) Reflectance of La_2O_3 and HfO_2 nanocomposites.

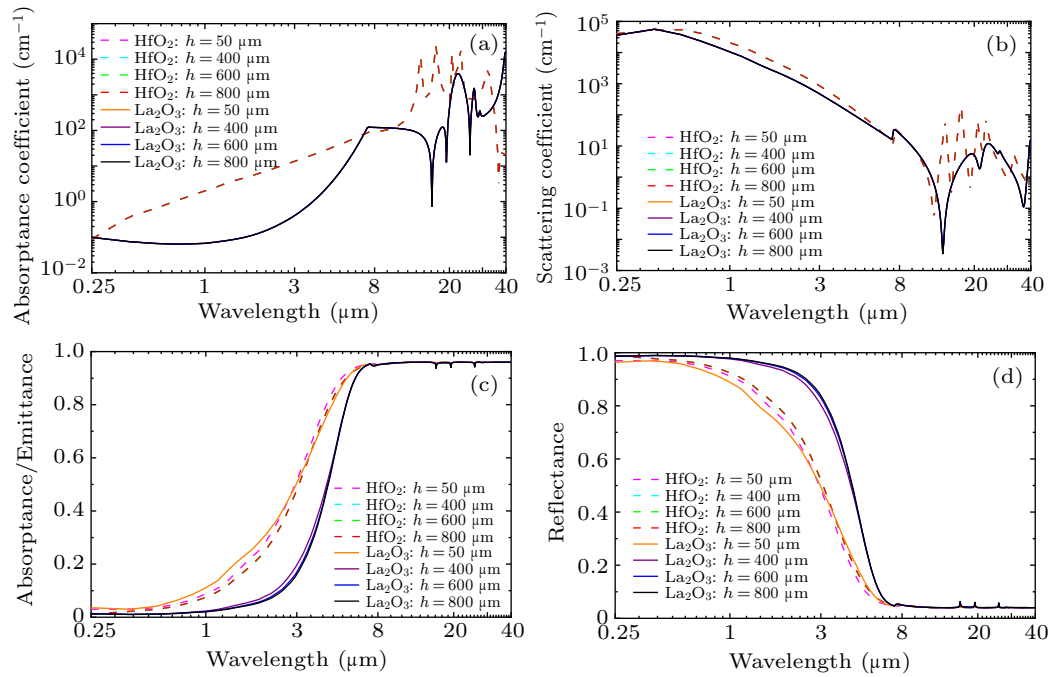


Fig. 13. Optical characteristics and corresponding optical properties of La_2O_3 and HfO_2 nanocomposites at various thicknesses with a fixed particle size ($d = 0.6$ μm) and volume fraction ($f_v = 40\%$). (a) Absorption coefficients of La_2O_3 and HfO_2 nanocomposites. (b) Scattering coefficients of La_2O_3 and HfO_2 nanocomposites. (c) Absorptance/emissivity of La_2O_3 and HfO_2 nanocomposites. (d) Reflectance of La_2O_3 and HfO_2 nanocomposites.

4. Conclusions

Our extensive exploration of the optical properties of La_2O_3 and HfO_2 nanocomposites across a broad spectrum underscores their potential for passive radiative cooling applications. Through a combination of multiscale simulations, including first-principles calculations and MC simulations, we comprehensively characterized the intrinsic optical constants at the atomic scale, as well as the scattering behavior and optical performance at the macroscale. The multiscale simulation method of first-principles calculation combined with MC simulation can quickly screen materials with specific optical properties in a high-throughput manner without being interfered by experimental conditions. In addition, because the bandgap is negatively correlated with reflectivity, materials with better radiative cooling performance can be found in the bandgap range of 4.96 eV to 5.39 eV. Furthermore, it is important to highlight that 3ph scattering significantly influences the mid-IR emissivity and must be carefully considered. Our findings provide valuable insights into the design and optimization of nanocomposites with robust optical properties, presenting a viable strategy to combat global warming through energy-efficient cooling solutions. However, our study did not consider the influence of temperature on the optical properties of the infrared band, including the possible lattice expansion caused by temperature, which affects the frequency shift effect and the effect of temperature on the damping factor γ_g. We suggest using molecular dynamics to introduce lattice constant correction at specified temperatures and incorporating temperature effect correction into three-phonon scattering to obtain more accurate optical performance prediction results. In addition, the MC simulation lacks a discussion of the emissivity under different particle size distributions. It is recommended to add optimization of the particle size distribution parameters in future research to obtain simulation results that are more in line with actual situations.

Acknowledgements

The authors gratefully acknowledge the National Natural Science Foundation of China (Grant Nos. U23A20565, 52301194, and 52101178), the Shanghai Science and Technology Commission (Grant No. 22511100400), the startup funding from Shanghai Jiao Tong University (Grant No. WH220405009), and Innovation Program of Shanghai Municipal Education Commission (Grant No. 2023ZKZD15) for providing funding support for this research.

References

[1] Mitchell J F B, Johns T C, Gregory J M and Tett S F B 1995 *Nature* **376** 501
[2] Goldstein E A, Raman A P and Fan S 2017 *Nat. Energy* **2** 1
[3] Raman A P, Anoma M A, Zhu L, Rephaeli E and Fan S 2014 *Nature* **515** 540
[4] Yin X, Yang R, Tan G and Fan S 2020 *Science* **370** 786
[5] Kośny J and Yarbrough D W 2022 *Thermal Insulation and Radiation Control Technologies for Buildings* (Cham: Springer International Publishing) pp. 1–35
[6] Yu X, Chan J and Chen C 2021 *Nano Energy* **88** 106259
[7] Zhao B, Hu M, Ao X, Xuan Q and Pei G 2020 *Appl. Energy* **262** 114548
[8] Wu M, Shao Z, Zhao N, Zhang R, Yuan G, Tian L, Zhang Z, Gao W and Bai H 2023 *Science* **382** 1379
[9] Oropeza-Perez I and Østergaard P A 2018 *Renew. Sustain. Energy Rev.* **82** 531
[10] Joannopoulos J D, Villeneuve P R and Fan S 1997 *Nature* **386** 143
[11] Lin K T, Han J, Li K, Guo C, Lin H and Jia B 2021 *Nano Energy* **80** 105517
[12] Zou C, Ren G, Hossain M M, Nirantar S, Withayachumnankul W, Ahmed T, Bhaskaran M, Sriram S, Gu M and Fumeaux C 2017 *Adv. Opt. Mater.* **5** 1700460
[13] Zhu B, Li W, Zhang Q, Li D, Liu X, Wang Y, Xu N, Wu Z, Li J, Li X, Catrysse P B, Xu W, Fan S and Zhu J 2021 *Nat. Nanotechnol.* **16** 1342
[14] Wang T, Wu Y, Shi L, Hu X, Chen M and Wu L 2021 *Nat. Commun.* **12** 365
[15] Chae D, Son S, Lim H, Jung P H, Ha J and Lee H 2021 *Mater. Today Phys.* **18** 100389
[16] Zhu L, Tian L, Jiang S, Han L, Liang Y, Li Q and Chen S 2023 *Chem. Soc. Rev.* **52** 7389
[17] Kim N K, Dutta S and Bhattacharyya D 2018 *Compos. Sci. Technol.* **162** 64
[18] Li X, Peoples J, Huang Z, Zhao Z, Qiu J and Ruan X 2020 *Cell Rep. Phys. Sci.* **1** 100221
[19] Xie Y, Wang L, Liu B, Zhu L, Shi S and Wang X 2018 *Mater. Des.* **160** 918
[20] Chen G, Wang Y, Qiu J, Cao J, Zou Y, Wang S, Jia D and Zhou Y 2020 *ACS Appl. Mater. Interfaces* **12** 54963
[21] Zheng J, Li Z, Zheng Y, Zhao W, Tan F, Yang F, Chen H and Xue L 2023 *Ceram. Int.* **49** 558
[22] Gao W and Chen Y 2023 *Small* **19** 220614
[23] Yang C, Fan H, Qiu S, Xi Y and Fu Y 2009 *J. Non-Cryst. Solids* **355** 33
[24] Al-Kuhaili M F 2004 *Opt. Mater.* **27** 383
[25] Zhao D, Chen Z and Liao X 2022 *Microstructures* **2** 2022007
[26] Banerjee W, Kashir A and Kamba S 2022 *Small* **18** 2107575
[27] Bilel C, Jbeli R, Ben Jemaa I, Dabaki Y, Alzaid M, Saadallah F, Bouaicha M and Amlouk M 2021 *J. Mater. Sci., Mater. Electron.* **32** 5415
[28] Lim S G, Kriventsov S, Jackson T N, Haeni J H, Schlom D G, Balbashov A M, Uecker R, Reiche P, Freeouf J L and Lucovsky G 2002 *J. Appl. Phys.* **91** 4500
[29] Vali R and Hosseini S M 2004 *Comput. Mater. Sci.* **31** 125
[30] Atuchin V V, Kalinkin A V, Kochubey V A, Kruchinin V N, Vemuri R S and Ramana C V 2011 *J. Vac. Sci. Technol. A* **29** 021004
[31] Tong Z, Peoples J, Li X, Yang X, Bao H and Ruan X 2022 *Mater. Today Phys.* **24** 100658
[32] Peoples J, Li X, Lv Y, Qiu J, Huang Z and Ruan X 2019 *Int. J. Heat Mass Transfer* **131** 487
[33] Blase X, Duchemin I, Jacquemin D and Loos P F 2020 *J. Phys. Chem. Lett.* **11** 7371
[34] Paul A M D and Niels H D B 1927 *Proc. R. Soc. Lond. A* **114** 243
[35] Polavarapu P L 2005 *J. Phys. Chem. A* **109** 7013
[36] Polavarapu P L 2005 *J. Phys. Chem. A* **109** 7013
[37] Hafner J 2008 *J. Comput. Chem.* **29** 2044
[38] Endot E, Sim P and Ismail S 2022 *Phys. Rev. B* **59** 7413
[39] Hammer B, Hansen L B, Nørskov J K, Heyd J and Scuseria G E 2004 *J. Chem. Phys.* **121** 1187
[40] Han Z, Yang X, Li W, Feng T and Ruan X 2022 *Comput. Phys. Commun.* **270** 108179
[41] Li W, Carrete J, A. Katcho N and Mingo N 2014 *Comput. Phys. Commun.* **185** 1747
[42] Redmond S, Rand S C, Ruan X L and Kaviany M 2004 *J. Appl. Phys.* **95** 4069
[43] Adachi G and Imanaka N 1998 *Chem. Rev.* **98** 1479

[44] Mehrotra P N, Chandrashekar G V, Rao C N R and Subbarao E C 1966 *Trans. Faraday Soc.* **62** 3586
[45] Kawamoto A, Jameson J, Griffin P, Kyeongjae Cho and Dutton R 2001 *IEEE Electron Device Lett.* **22** 14
[46] Jiang T T, Sun Q Q, Li Y, Guo J J, Zhou P, Ding S J and Zhang D W 2011 *J. Phys. Appl. Phys.* **44** 185402
[47] Zhao X and Vanderbilt D 2002 *Phys. Rev. B* **65** 233106
[48] Damien C 2020 V_Sim
[49] Scarel G, Debernardi A, Tsoutsou D, Spiga S, Capelli S C, Lamagna L, Volkos S N, Alia M and Fanciulli M 2007 *Appl. Phys. Lett.* **91** 102901
[50] Zhao X and Vanderbilt D 2002 *Phys. Rev. B* **65** 075105
[51] Feinberg A and Perry C H 1981 *J. Phys. Chem. Solids* **42** 513
[52] Bright T J, Watjen J I, Zhang Z M, Muratore C and Voevodin A A 2012 *Thin Solid Films* **520** 6793
[53] Paulick T C 1986 *Appl. Opt.* **25** 562
[54] Armelao L, Pascolini M, Bottaro G, Bruno G, Giangregorio M M, Losurdo M, Malandrino G, Lo Nigro R, Fragalà M E and Tondello E 2009 *Phys. Chem. C* **113** 2911
[55] Smith D and Baumeister P 1979 *Appl. Opt.* **18** 111
[56] Medford R D, Powell A L T and Fletcher W H W 1962 *Nature* **196** 32
[57] Adachi S 1999 *Optical Properties of Crystalline and Amorphous Semiconductors: Materials and Fundamental Principles* (Boston, MA: Springer US) pp. 33–62
[58] Ribbing C G and Wäckelgård E 1991 *Thin Solid Films* **206** 312